

Pore-scale Modeling of Viscous Flow and Induced Forces in Dense Sphere Packings

Bruno Chareyre · Andrea Cortis · Emanuele Catalano · Eric Barthélemy

Received: date / Accepted: date

Abstract We propose a method for effectively upscaling incompressible viscous flow in large random polydispersed sphere packings: the emphasis of this method is on the determination of the forces applied on the solid particles by the fluid. Pore bodies and their connections are defined locally through a regular Delaunay triangulation of the packings. Viscous flow equations are upscaled at the pore level, and approximated with a finite volume numerical scheme. We compare numerical simulations of the proposed method to detailed finite element (FEM) simulations of the Stokes equations for assemblies of 8 to 200 spheres. A good agreement is found both in terms of forces exerted on the solid particles and effective permeability coefficients.

Keywords viscous flow, granular material, solid fluid coupling, pore-network, finite volumes

1 Introduction

Understanding the mechanical behavior of fluid-saturated granular systems (e.g., soils, rocks, concretes, powders, and chemical reactors) hinges upon a detailed description of the stress exchange between fluid and solid phases. Fluid flowing through a matrix of solid spheres, exerts forces on the solid grains, displacing them from the trajectory they would have had if

Bruno Chareyre
Grenoble INP, UJF Grenoble I, CNRS UMR 5521, 3SR lab
BP53, 38041 Grenoble Cedex 9, France
E-mail: bruno.chareyre@grenoble-inp.fr

Andrea Cortis
Earth Sciences Division
Lawrence Berkeley National Laboratory
Berkeley, CA, 94806, U.S.A.

Emanuele Catalano
Grenoble INP, UJF Grenoble I, CNRS UMR 5521, 3SR lab
BP53, 38041 Grenoble Cedex 9, France

Eric Barthélemy
Grenoble INP, UMR CNRS 5519, LEGI
BP 53, 38041 Grenoble Cedex 9, France

List of Symbols

α	Non dimensional conductance factor
Ω	Full domain of the two-phase problem
Ω_i	Domain defined by tetrahedron i
Ω_{ij}	union of tetrahedra (S_{ij}, P_i) and (S_{ij}, P_j)
Γ	Part of Ω occupied by the solid phase
Γ_i	Domain occupied by solid particle i
Θ	Part of Ω occupied by the fluid phase (pore space)
Θ_i	Part of Ω_i occupied by the fluid phase (pore)
Θ_{ij}	part of Ω_{ij} occupied by the fluid phase (throat)
S_{ij}	surface of the facet ij , separating tetrahedra i and j
∂X	contour of domain X
$\partial^f X$	part of contour of X intersecting the fluid phase
$\partial^s X$	part of contour of X intersecting (or in contact with) the solid phase
γ_{ij}	area of $\partial\Theta_{ij}$ in contact with spheres
γ_{ij}^k	area of the part of $\partial\Theta_{ij}$ in contact with sphere k
S_{ij}	the common facets of tetrahedra Ω_i and Ω_j
A_{ij}^f	area of the fluid part $S_{ij} \cap \Theta$ of facet ij
A_{ij}^k	area of the intersection $S_{ij} \cap \Gamma_k$ of facet ij and sphere k
P_i	Voronoi dual (weighted center) of tetrahedra i
p^f	microscopic (pore-scale) fluid pressure
p_i	macroscopic fluid pressure in tetrahedra i
\mathbf{u}^f	microscopic fluid velocity
\mathbf{u}	macroscopic fluid velocity
\mathbf{v}	geometric contour velocity
q_{ij}	flux through facet ij
V_i^f	fluid volume contained in pore i
R_{ij}^h	hydraulic radius of throat ij
R_{ij}^{eff}	effective radius of throat ij
μ	dynamic viscosity
L_{ij}	length of throat ij
F_x^y	forces exerted by the fluid on the solid phase, x and y denote different terms in forces decomposition
g_{ij}	hydraulic conductance of facet (throat) ij
K_{ij}	hydraulic conductivity of facet (throat) ij

left to interact alone in a dry medium. In turn, the displacement of the grains creates a dynamically changing domain for the fluid flow. The combination of these two effects results in nontrivial physically measurable effects, which are hard to capture by first-principles derivations alone. Despite the important practical applications that are touched by fluid-saturated granular systems, no model currently exists that can efficiently reproduce the precise evolution of large systems over different stress conditions in 3D problems.

This work represents a first step in the direction of developing a fully-coupled, computationally efficient model for the evolution of fluid-saturated granular materials under stress. In particular, we will focus our effort on the faithful approximation of the forces applied by the fluid on the solid grains, with the aim of incorporating these forces in the *discrete element method* (DEM) computations Cundall and Strack 1979.

While the movement of the solid grains can be efficiently modeled by DEM computations, viscous fluid computations in dynamically changing domains present incredible computational challenges. At the microscopic (sub-pore) scale, fluid flow is governed by Stokes equations, which express fluid mass and momentum conservation at small Reynolds and

Stokes numbers:

$$\nabla p = \mu \nabla^2 \mathbf{u} - \rho \nabla \Phi, \quad (1)$$

$$\nabla \cdot \mathbf{u} = 0 \quad (2)$$

where \mathbf{u} , and p are the microscopic fluid velocity and piezometric pressure, respectively, μ is the fluid dynamic viscosity, and Φ is a potential field (e.g., gravitational field). The piezometric pressure p is related to the absolute pressure p^* via $p = p^* - \rho \Phi$. Equations (1)-(2) are augmented with a no-slip boundary condition for the fluid velocity, at the grain boundaries, $\mathbf{u} = 0$, which is essentially responsible for the microscopic viscous energy losses (drag) that translate in a net loss of the macroscopic piezometric pressure, p , over the length of a porous column.

At centimeter scale (and above), for relatively homogeneous porous materials, fluid flow is governed by Darcy law, which states the linear proportionality between the macroscopic pressure gradient ∇p and the fluid flux q (discharge per unit area) :

$$q = -\frac{k}{\mu} \nabla p, \quad (3)$$

where k is the permeability. Darcy law emerges as a volume averaging of the viscous forces applied by the fluid flow at the surface of the grains over a sufficiently large number of pores.

Recent advances in porous media imaging techniques give access to an unprecedented level of pore-space detail, down to the micrometer scale and below, where the Stokes equations could be, in principle, solved numerically. The numerical solution of the Stokes equations in spheres assemblies is, however, computationally expensive, and becomes prohibitive on commodity desktop computers for number of particles exceeding the hundreds. On the other hand, typical DEM simulations, can easily handle assemblies with number of particles ranging between 10^4 and 10^5 on the same commodity desktop computers, and compute their evolution over 10^5 time-steps or more (see e.g. Scholtes et al. 2009). It is therefore obvious that a direct coupling of Stokes equations and DEM simulations becomes unfeasible for real-world problems, hence the need to develop an upscaled fluid model that minimizes the ratio between the degrees of freedom (DOFs) in the fluid and the number of solid particles.

The past thirty years have seen a considerable effort in the exact upscaling of Equations (1)-(2), i.e., on how to obtain expressions for the permeability k from the knowledge of the microscopic flow. Upscaling techniques such as the Volume Averaging with Closure (Whitaker 1999), and homogenization (Sanchez-Palencia and Zaoui 1987) invariably require the solution of a (tensorial) Stokes problem, which has essentially the same algorithmic complexity of the ‘‘original’’ Stokes fluid flow problem. In this work we will not be concerned with this type of theoretical upscaling issues. Rather, we will focus our attention to the derivation of a physically based, simplified model of flow through porous materials that overcomes the numerical issues associated with the solution of the full Stokes problem.

Different strategies have been adopted in the past for the solution of the fluid-solid coupling, which essentially differ in the modeling techniques adopted for the fluid part of the problem, as reviewed below.

Microscale Stokes flow modeling

The numerical solution of the Stokes equations is a computationally demanding task, especially for complex three-dimensional pore geometries. Finite Element Methods (FEMs) are often used because of their flexibility in the definition of the numerical mesh. FEM meshes

in three dimensions tend to be, however, very large and so do the computer memory footprint and computational times needed for the solution of the associated nonlinear system of equations. Glowinski et al. (2001), for instance, reported computational costs of approximately 0.1s per particle and per time-step in fluidization simulations on a SGI Origin 2000, employing an advanced fictitious domain method and a partially parallelized code: extrapolating these values to a number of particle typical of DEM problems, results in computational times in the order of 3-30 years.

A numerical method that does not resort to the solution of large systems of nonlinear equations is the Lattice-Boltzmann (LB) scheme. While LB is generally faster than the FEM and has the possibility of being easily parallelized on multicore machines and GPUs (<http://sailfish.us.edu.pl/>), commonly implemented fixed size grids can result in considerably larger computer memory occupancy in three dimensions. Only recently, grid refinement schemes have started to be implemented in open source LB codes (<http://www.lbmethod.org/palabos/>). Realistic microscale flow simulations in complex pore geometries still require, however, access to large CPU clusters.

Continuum-discrete Darcy flow modeling

In order to get acceptable computational costs, a number of authors considered coarse-grid CFD methods (Nakasa et al. 1999; Kawaguchi et al. 1998; McNamara et al. 2000; Kafui et al. 2002; Zeghal and Shamy 2004; Niebling et al. 2010). In such methods, flow and solid-fluid interactions are defined with simplified semi-empirical models based on Darcy law. There is no direct coupling at the local scale: the forces acting on the individual particles are defined as a function of mesoscale-averaged fluid velocity obtained from porosity-based estimates of the permeability. Such strategies have been adopted for dilute particles suspensions as well as for dense materials at low strain rate (e.g., soils, rocks). Continuum-discrete couplings succeed in making coupled problems affordable in terms of CPU cost. The use of phenomenological laws for the estimation of the permeability, however, limits severely the predictive power of these models in uncalibrated parameter regions. Ultimately, such strategies do not render correctly the individual particle behavior, and cannot be reliably applied to problems such as strain localization, segregating phenomena, effects of local heterogeneities in porosity, and internal erosion by transport of fines.

Pore-network modeling

Pore-network modeling covers a third class of models, based on a simplified representation of porous media as a network of pores and throats. Pore-network models have been most commonly developed to predict the permeability of materials from microstructural geometry (Bryant et al. 1993; Thompson and Fogler 1997; Bakke and Øren 1997; Patzek and Silin 2001; Hilpert et al. 2003; Abichou et al. 2004), but have also been extended to include multiphase flow effects (e.g., air bubbles, immiscible two-phase flow) (Bryant and Blunt 1992; Øren et al. 1998; Bryant and Johnson 2003; Piri and Blunt 2005). Crucial for their success is an adequate definition of how fluids are exchanged between pores in term of the local pore geometry. This aspect will be discussed further in section 2.2.2.

Deformable pore-network modeling

Pore-network models studies have mostly focused on flow in passive rigid solid frames. Little attention, however, has been devoted to the definition of forces applied to individual particles in the solid phase. The main aim of this work is to develop expressions for these forces, to be used in three-dimensional DEM simulations of solid particles immersed in a fluid flow.

Early ideas of a coupled pore-network flow and DEM can be found in the works of Hakuno and Tarumi (1995) and later by Bonilla (2004). These studies, however, were limited to 2D models of discs assemblies, where pores were defined by closed loops of particles in contact. Since such pore geometry does not offer any free path for fluid exchanges, 2D problems implied some arbitrary definition of the local conductivity, assuming virtual channels between adjacent voids. Adapting this approach to 3D spheres assemblies enables the definition of the local hydraulic conductivity using the actual geometry of the packing, as spheres packings always define an open network of connected voids. This in turns opens up the possibility of predicting both the macro-scale permeability and the forces acting on the individual particles rather than postulating it: this is the central theme of this work.

2 Upscaled fluid flow model

As described in the previous section, fine-scale Stokes flow numerical simulations present a prohibitive computational cost and an effective, upscaled fluid flow model is needed. In this section, we present a detailed derivation of the proposed upscaled fluid flow model, starting from the decomposition of the pore space in terms of pore bodies and local conductances. This decomposition results naturally in a finite volume description of the flow equations. The expressions for the forces on the individual particles are then derived. Finally, we describe the actual implementation of the model.

2.1 Pore-scale volume decomposition

Delaunay triangulations and their dual Voronoi graphs are widely used for structural studies of molecules, liquids, colloids, and granular materials (Aurenhammer 1991). More specifically, it has been applied to domain decompositions in sphere packings, for the definition of microscale strains and stresses (Calvetti et al. 1997; Bagi 2006; Jerier et al. 2010), and pore-scale modeling of single-phase or multi-phase flow (Bryant and Blunt 1992; Bryant and Johnson 2003; Thompson and Fogler 1997). The most common type of Delaunay triangulation (hereafter referred to as *classical Delaunay*) is defined for a set of isolated points. In this case the dual *classical Voronoi* graph of the triangulation defines polyhedra enclosing each point in the set, and facets of the polyhedra are parts of planes equidistant to two adjacent points. For mono-sized spheres, this construction gives a map of the void space. Classical Delaunay-Voronoi graphs, however, present a number of misfeatures when applied to spheres of different sizes. Notably, branches and facets of the Voronoi graph can cross non-void regions, or divide regions in such a way that the splits are orthogonal to the actual void, as illustrated in fig. 1.

Luchnikov et al. 1999 proposed to define the split between spheres by means of curved surfaces equidistant from both spheres surfaces, thus defining *Voronoi S* cells. The use of Voronoi S graphs is, however, computationally expensive for large number of particles. *Regular Delaunay* triangulation (see fig. 1), while overcoming the problems associated with classical Delaunay triangulations, provides a computationally cheap alternative to the use of Voronoi S cells.

Regular Delaunay triangulation (Edelsbrunner and Shah 1996) generalizes classical Delaunay triangulation to weighted points, where weights account for the radius of spheres. It can be shown that the dual Voronoi graph of the regular triangulation is entirely contained in voids between spheres, as opposed to the dual of classical Delaunay, as seen on fig. 1 (2D)

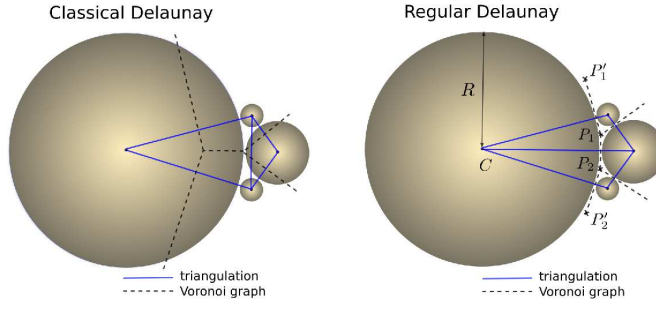


Fig. 1 Comparison of 2D triangulations and dual Voronoi graphs obtained from classical Delaunay and regular Delaunay: classical Voronoi graph has branches inside discs, while regular Voronoi gives all branches in the voids space. Observe that if R tends to infinity, $\{P_1', P_2, P_2'\}$ tends to aligned points.

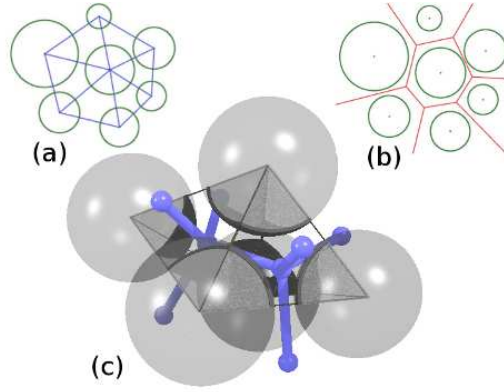


Fig. 2 Adjacent tetrahedra in the regular Delaunay triangulation and dual Voronoi network, in two dimensions (a,b) and three dimensions (c).

and fig. 2 (2D/3D). Edges and facets of the regular Voronoi graph are lines and planes, thus enabling fast computation of geometrical quantities. In section 2.2.2 we will use a combination of regular Delaunay facets and regular Voronoi vertices to decompose the pore volume.

In what follows, Ω denotes a domain occupied by a porous material, in which Γ and Θ are the domains occupied respectively by the solid and the fluid: $\Omega = \Gamma \cup \Theta$, $\Gamma \cap \Theta = \emptyset$ (Θ is also called *pore space*). We denote by N_c the number of tetrahedral cells in the regular Delaunay triangulation of the sphere packing, and Ω_i the domain defined by tetrahedron i : $\Omega = \cup_{i=1}^{N_c} \Omega_i$. Similarly, N_s is the number of spheres, and Γ_i the domain occupied by sphere i , so that $\Gamma = \cup_{i=1}^{N_s} \Gamma_i$.

2.2 Fluxes

2.2.1 Continuity

We define Θ_i as the portion of the tetrahedral element Ω_i not occupied by spheres. The volume V_i^f of Θ_i is filled by fluid (fig. 3), since we are considering saturated porous media.

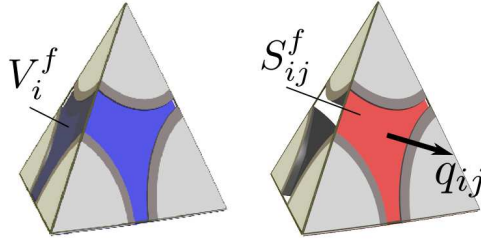


Fig. 3 Tetrahedral element of the finite volume decomposition.

The continuity equation for an incompressible fluid (2), cast into its surface integral form and using the divergence theorem, gives a relation between the time derivative of V_i^f and the fluid velocity:

$$\dot{V}_i^f = \int_{\partial\Theta_i} (\mathbf{v} - \mathbf{u}) \cdot \mathbf{n} \, ds, \quad (4)$$

where $\partial\Theta_i$ is the contour of Θ_i , \mathbf{n} the outward pointing unit vector normal to $\partial\Theta_i$, \mathbf{u} the fluid velocity, and \mathbf{v} the velocity of the contour. One part of the contour, noted $\partial^s\Theta_i$, corresponds to a solid-fluid interface. At any point in $\partial^s\Theta_i$, we have $(\mathbf{v} - \mathbf{u}) \cdot \mathbf{n} = 0$, so that the integration domain above can be restricted to $\partial^f\Theta_i$, the fluid part of the contour. By introducing $S_{ij}^f (j \in \{j_1, j_2, j_3, j_4\})$ the intersections of triangular surfaces S_{ij} with the fluid domain (fig. 3), so that $\partial^f\Theta_i = \cup_{j=j_1}^{j_4} S_{ij}^f$, we can define four intergrals describing fluid fluxes q_{ij} from tetrahedron i to adjacent tetrahedra j_1 to j_4 . Finally:

$$\dot{V}_i^f = \sum_{j=j_1}^{j_4} \int_{S_{ij}^f} (\mathbf{v} - \mathbf{u}) \cdot \mathbf{n} \, ds = - \sum_{j=j_1}^{j_4} q_{ij} \quad (5)$$

In deformable sphere packings, \dot{V}_i^f can be computed on the basis of particles motion (i.e. velocities of the vertices of the tetrahedra), thus linking fluid fluxes with the deformation of the solid skeleton. The derivation of \dot{V}_i^f as function of particles velocities is not detailed here for brevity, because in what follows particles are assumed to be fixed: V_i^f is constant and the continuity equation simplifies to

$$\sum_{j=j_1}^{j_4} q_{ij} = 0. \quad (6)$$

2.2.2 Local conductance

Both Stokes (1) and Darcy (3) equations imply a linear relation between pressure gradients and fluxes. Here, we introduce a *inter-pore* gradient, defined as the ratio between pressure difference $p_i - p_j$ between two connected tetrahedral cells, and a relevant length L_{ij} - to be defined below. Being linear, the relation between q_{ij} and the inter-pore gradient can be expressed using the *local conductance* factor g_{ij} of facet ij :

$$q_{ij} = g_{ij} \frac{p_i - p_j}{L_{ij}}. \quad (7)$$

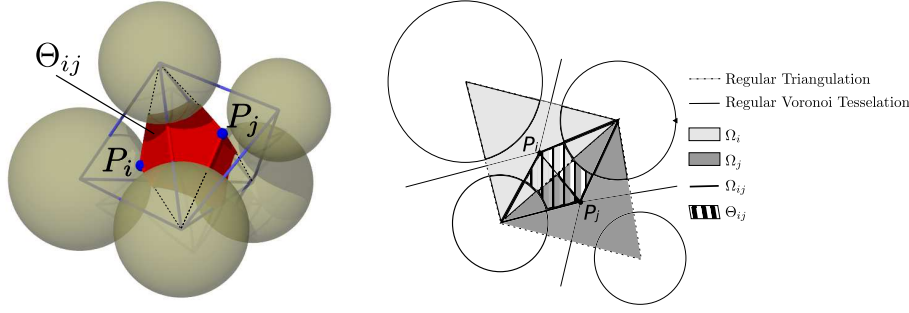


Fig. 4 Construction of subdomain Θ_{ij} , defining the volume of the throat assigned to a facet for the definition of hydraulic radius R_{ij}^h ; in 3D (left) and 2D (right).

Considerable efforts have been devoted in the past literature to the definition of g_{ij} in pore-network models, with attempts to generalize Poiseuille's law to pores of different shapes, eventually mapping the microstructure of some real materials for permeability predictions (Piri and Blunt 2005; Hilpert et al. 2003). By analogy with the Hagen-Poiseuille relation, g_{ij} may be defined by introducing the *hydraulic radius* of the pore throat R_{ij}^h , and its cross-sectional area A_{ij} (the definitions of R_{ij} and A_{ij} are discussed below), by means of a non-dimensional conductance factor α reflecting the throat's shape (Hagen-Poiseuille for circular cross-sections of radius $2R_{ij}^h$ is recovered with $\alpha = 1/2$):

$$g_{ij} = \alpha \frac{A_{ij} R_{ij}^{h2}}{\mu}. \quad (8)$$

L_{ij} , R_{ij}^h , and A_{ij} are geometrical quantities describing the throats geometry. Even though these variables are found in most of the papers cited above, there is no general agreement on their definition for pore-network modeling of arbitrary microstructural geometry. A detailed analysis of the effect of non-circular cross-sections with variable constriction along the flow path can be found in Patzek and Silin 2001 and Mortensen et al. (2005), while Thompson and Fogler (1997), Bakke and Øren (1997), and Bryant et al. (1993) focused specifically on triangulated sphere packings. Some of these models, however, do not clearly define a partition of the void space, and as such they need ad-hoc corrections for L_{ij} to ensure that the same pore volumes are not accounted for multiple times in different cells (Bryant et al. 1993). We observe here that in *classical* Delaunay-Voronoi graphs of spheres with polydispersed radii, circumcenters (and barycenters) may lie inside the solid phase (Bryant and Blunt (1992)), and definitions of L_{ij} based on distances between circumcenters become problematic.

For the present model, we take advantage of the regular Voronoi graph structure, whose edges and vertices are always contained in the pore space. A partition of the full domain is defined as the set of sub-domains Ω_{ij} , with Ω_{ij} the union of two tetrahedra constructed from facet S_{ij} and Voronoi vertices P_i and P_j : $\Omega_{ij} = (S_{ij}, P_i) \cup (S_{ij}, P_j)$. Keeping only the part of Ω_{ij} that intersect the pore space, we define a throat connecting two pores, noted Θ_{ij} (see figs. 4 and 5). We define the hydraulic radius R_{ij}^h in eq. 8 as the ratio between the throat's volume and solid-fluid interfaces area. Denoting by ϕ_{ij} the volume of Θ_{ij} , and γ_{ij} the area of $\partial^s \Theta_{ij}$ (the part of the contour in contact with spheres), the *hydraulic radius* R_{ij}^h reads:

$$R_{ij}^h = \phi_{ij} / \gamma_{ij} \quad (9)$$

Note that, with the partition of the voids space proposed here, the definition of effective radii accounts for the exact total solid surface and void volume in the packing. Noting \mathcal{F} the set of facets, we have $\Theta = \bigcup_{ij \in \mathcal{F}} \Theta_{ij}$, and $\partial\Theta = \bigcup_{ij \in \mathcal{F}} \partial^s \Theta_{ij}$.

We define the length of the throat as the distance between Voronoi vertices: $L_{ij} = \|P_i P_j\|$, and the throat's cross-sectional area as that of the fluid domain S_{ij}^f introduced in the previous section (fig. 3). In this model, the factor α is uniquely assigned to all throats of a packing and can be considered a calibration factor. A value of $\alpha = 1/2$ has been chosen as an initial guess, by analogy with the Hagen-Poiseuille law. The numerical simulations presented in section 3 indicate that setting $\alpha=1/2$ is indeed appropriate for the spheres geometries considered in this investigation. We observe that the values of α obtained analytically vary in a moderately wide range of values for compact throats sections (Patzek and Silin 2001). It is also worth noting that, the factor α being the same for all throats, modifying this value will not modify the pressure distribution in the boundary value problems presented below (mixed Neumann-Dirichlet), and consequently it would not affect the values of forces applied on the particles.

Another possible definition of g_{ij} has been proposed by Bryant and Blunt (1992) for dense packings of mono-sized spheres. These authors defined g_{ij} as a function of an *effective radius* R_{ij}^{eff} (ER), accounting thus only for the effects of the narrowest cross-section (surface S_{ij} in fig. 3) and disregarding the influence of the full volume of the flow path. The effective radius is defined¹ as $R_{ij}^{eff} = (r_{ij}^{eq.} + r_{ij}^{inscr.})/4$, where $r_{ij}^{eq.}$ is the radius of the disk of same surface as S_{ij}^f , and $r_{ij}^{inscr.}$ is the radius of the circle inscribed in the three spheres intersecting the facet. It represents the hydraulic radius of the circular tube that would have the same conductance as the throat:

$$g_{ij} = \frac{2\pi R_{ij}^{eff4}}{\mu} = \frac{A_{ij}^{eff} R_{ij}^{eff2}}{2\mu}, \quad (10)$$

where $A_{ij}^{eff} = \pi(2R_{ij}^{eff})^2$ is the cross-sectional area of the equivalent tube. The second expression is given for the purpose of comparison with eq. 8. The values of R_{ij}^h and R_{ij}^{eff} in random dense packings of polydispersed spheres, and the results they give in terms of fluxes and forces are compared in section 3.

2.3 Forces on solid particles

The total force \mathbf{F}^k generated on particle k by the fluid includes the effects of absolute pressure p^* and viscous stress τ , which divergence is the right-hand side of (1):

$$\mathbf{F}^k = \int_{\partial\Gamma_k} (p^* \mathbf{n} + \tau \mathbf{n}) \, ds. \quad (11)$$

We recall that the piezometric pressure governing the flow problem was defined as $p = p^* - \rho\Phi(\mathbf{x})$. By introducing p in the previous equation, one can define \mathbf{F}^k as the sum of three terms, noted $\mathbf{F}^{b,k}$, $\mathbf{F}^{p,k}$ and $\mathbf{F}^{v,k}$:

$$\mathbf{F}^k = \int_{\partial\Gamma_k} \rho\Phi(\mathbf{x}) \mathbf{n} \, ds + \int_{\partial\Gamma_k} p \mathbf{n} \, ds + \int_{\partial\Gamma_k} \tau \mathbf{n} \, ds = \mathbf{F}^{b,k} + \mathbf{F}^{p,k} + \mathbf{F}^{v,k}. \quad (12)$$

¹ For the convenience of comparisons, and consistently with the expression of conductance we are using, we introduce the effective radius R^{eff} as the half of its definition in the original paper from Bryant and Blunt. The final value of the conductance is preserved.

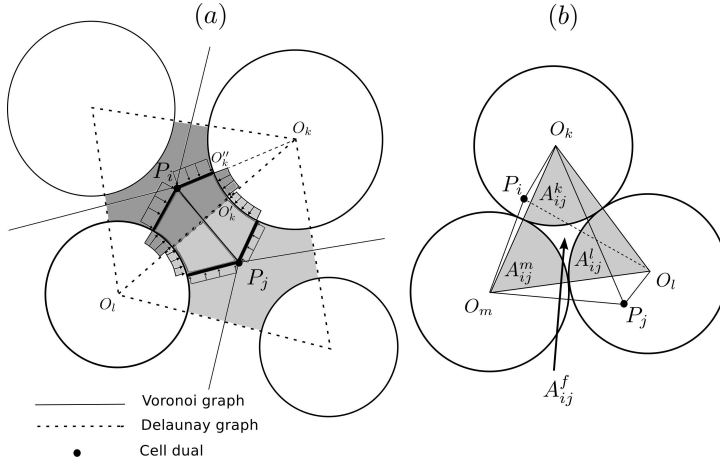


Fig. 5 Volume decomposition for viscous drag force definition : (a) pressure distribution on $\partial\Omega_{ij}$ (in 2D for clarity), (b) definition of facet-spheres intersections in 3D.

$\mathbf{F}^{b,k}$ is the so-called *buoyancy* force, and can be computed independently. In the case of gravitational body forces, it will give the Archimede's force proportional to the volume of Γ_k . $\mathbf{F}^{p,k}$ and $\mathbf{F}^{v,k}$ are terms resulting from viscous flow: $\mathbf{F}^{p,k}$ resulting from losses of piezometric pressure, and $\mathbf{F}^{v,k}$ resulting from viscous shear stress. Both $\mathbf{F}^{p,k}$ and $\mathbf{F}^{v,k}$ will be derived separately, at the scale of the domains Ω_{ij} that were introduced in the previous section, in the approximation of piecewise constant pressure.

2.3.1 Integration of pressure

The force generated by p on particle k in domain Ω_{ij} is the sum of two terms implying pressures p_i and p_j (see fig. 5),

$$\mathbf{F}_{ij}^{p,k} = \int_{\partial\Gamma_k \cap \Omega_{ij} \cap \Omega_{ij}} p_i \mathbf{n} ds + \int_{\partial\Gamma_k \cap \Omega_{ij} \cap \Omega_{ij}} p_j \mathbf{n} ds \quad (13)$$

In three dimensions, computing such integral on spherical triangles could be computationally expensive. It is more convenient to project the pressure on the conjugate planar parts (angular sectors) of the closed domain $\Gamma_k \cap \partial\Omega_{ij}$, which trace in the plane of fig. 5 corresponds to segments OO' and OO'' . Note that when iterating over all domains Ω_{ij} adjacent to one particle, the integral on sectors of type OO'' will appear twice with opposite normals and cancel out each other. Finally, the contribution to pressure force on particle k in domain Ω_{ij} is simply proportional to the area A_{ij}^k of sector $S_{ij} \cap \Gamma_k$ (trace OO'). If \mathbf{n}_{ij} is the unit vector pointing from P_i to P_j , the force reads:

$$\mathbf{F}_{ij}^{p,k} = A_{ij}^k (p_i - p_j) \mathbf{n}_{ij} \quad (14)$$

2.3.2 Integration of viscous stresses

To integrate the viscous stresses, we first define the total viscous force \mathbf{F}_{ij}^v , applied on the solid phase in Ω_{ij} . Since Ω_{ij} intersects three spheres, \mathbf{F}_{ij}^v will have to be later splitted into

three terms. \mathbf{F}_{ij}^v is defined as

$$\mathbf{F}_{ij}^v = \int_{\partial^s \Theta_{ij}} \boldsymbol{\tau} \mathbf{n} \, ds. \quad (15)$$

An expression of \mathbf{F}_{ij}^v is obtained by integrating the momentum conservation equation (1) in Θ_{ij} . The integral is cast in the form of a surface integral on contour $\partial \Theta_{ij}$ using the divergence theorem :

$$\int_{\partial \Theta_{ij}} (p \mathbf{n} + \boldsymbol{\tau} \mathbf{n}) \, ds = 0.$$

This integral can be decomposed as in eq. 16, where the terms correspond respectively to \mathbf{F}_{ij}^v , to the sum of viscous stress on the fluid part $\partial^f \Theta_{ij}$ of the contour, and to the sum of pressure. By neglecting the second term (thus assuming that pressure gradients are equilibrated mainly by viscous stress on the solid phase), the expression of \mathbf{F}_{ij}^v takes the form of equation 17, where the viscous force is simply proportional to the product of the throat's cross-sectional area A_{ij}^f and the pressure jump $p_j - p_i$.

$$\int_{\partial^s \Theta_{ij}} \boldsymbol{\tau} \mathbf{n} \, ds + \int_{\partial^f \Theta_{ij}} \boldsymbol{\tau} \mathbf{n} \, ds + \int_{\partial \Theta_{ij}} p \mathbf{n} \, ds = 0. \quad (16)$$

$$\mathbf{F}_{ij}^v \simeq - \int_{\partial \Theta_{ij}} p \mathbf{n} \, ds = A_{ij}^f (p_j - p_i) \mathbf{n}_{ij} \quad (17)$$

In order to define the viscous forces applied on each of the three spheres intersecting Ω_{ij} , it is assumed that the force on sphere k is proportional to the surface of that sphere contained in the subdomain. If γ_{ij}^k denotes the area of the curved surface $\partial \Gamma_k \cap \Omega_{ij}$, the force on k then reads:

$$\mathbf{F}_{ij}^{v,k} = \mathbf{F}_{ij}^v \frac{\gamma_{ij}^k}{\sum_{k=1}^3 \gamma_{ij}^k} \quad (18)$$

Finally, the total force on one particle is obtained by summing viscous and pressure forces from all incident facets with the buoyancy force:

$$\mathbf{F}^k = \sum_{(ij) \text{ incident}} \{ \mathbf{F}_{ij}^{v,k} + \mathbf{F}_{ij}^{p,k} \} + \mathbf{F}^{b,k} \quad (19)$$

2.4 Implementation

2.4.1 Network definition

The network model has been implemented in C++, and it is freely available as an optional package of the open-source software Yade (Smilauer et al. 2010). The C++ library CGAL (Boissonnat et al. 2002) is used for the triangulation procedure. This library ensures exact predicates and constructions, and is one of the fastest computational geometry codes available (Liu and Snoeyink 2005). It is worth noting that regular triangulation involves only squared distances comparisons, thus avoiding time consuming square roots and divisions. The computation of forces (eq. 19) also requires only simple vector multiplications. The only non-trivial operation is the computation of solid angles needed to define the volumes and surfaces associated to sphere-tetrahedron intersections, in eq.9. This cost can be reduced significantly, however, using the algorithm of Oosterom and Strackee (1983).

2.4.2 Flux problem solution

Combining Equations 6 and 7 gives for element i :

$$\sum_{j=1,\dots,4} \frac{g_{ij}}{L_{ij}} (p_i - p_j) = \sum_{j=1,\dots,4} K_{ij} (p_i - p_j) = \dot{V}_i^f \quad (20)$$

If the triangulation defines N_c tetrahedra and if the number of elements with imposed pressure is N_p , the pressure field is obtained after solving a linear system of size $N_c - N_p$. The matrix of the system is sparse and symmetric ($K_{ij} = K_{ji}$), and positive defined. An over-relaxed Gauss-Siedel algorithm has been used to solve this linear system in the simulations presented below. This algorithm has been chosen for its simplicity, though other strategies could be preferred in the future for better performance and for complex couplings (including particles motion).

3 Comparison with small-scale FEM simulations

3.1 Numerical setup

In this section, we compare the results of the pore-scale finite volume (FV) formulation described in section 2 with FEM Stokes flow simulations of Equ. (1)-(2), for dense sphere packings subjected to an imposed pressure gradient. We consider sphere packings contained in a cube of size l_0 (all results below will be normalized with respect to this reference length). Boundaries are accounted for in the triangulation process in the form of spheres with near-infinity radii ($10^6 \times l_0$). Hence, planes are not introducing special cases to handle in the algorithms, and equations presented in previous section apply for boundaries as for any other sphere.

The smallest test problem we consider is a regular cubic packing of 8 spheres. Packings of nine spheres are obtained by placing an additional sphere (with variable size d) in the center of the cubic packing (fig. 6). Larger assemblies of 25, 54, and 200 spheres (fig. 7) are random packings that were generated using the DEM software Yade (Smilauer et al. 2010) by simulating the growth of spheres after random positioning, using the algorithm of Chareyre et al. (2002). Radii are generated randomly with respect to uniform distributions between radii r_{min} and r_{max} . In the 200-spheres assembly, sizes are narrow graded, with $r_{min}/r_{max} = 0.9$ (this small dispersion of sizes prevents the formation of crystal-like patterns). Sizes in the 25-spheres and 54-spheres packings, are more dispersed, with $r_{min}/r_{max} = 0.5$. After dense and stable packings are obtained, the spheres's positions are fixed.

For each packing geometry, the flow boundary conditions are the ones described on fig. 6: pressure is imposed on the top and bottom boundaries, while no-flux conditions are imposed on the lateral boundaries.

Both “no-slip” and “symmetry” conditions are considered on the lateral boundaries. In the FV modeling, they are reflected in the definition of conductivity and forces in the throats Θ_{ij} in contact with boundaries as follows:

- For the “no-slip” condition, the surfaces of infinite spheres in contact with Θ_{ij} are accounted for in Eqs. 9 and 18, as for any other sphere.
- For the “symmetry” condition, these surfaces are ignored : $\gamma_{ij}^k = 0$, when k is the indice of a bounding sphere.

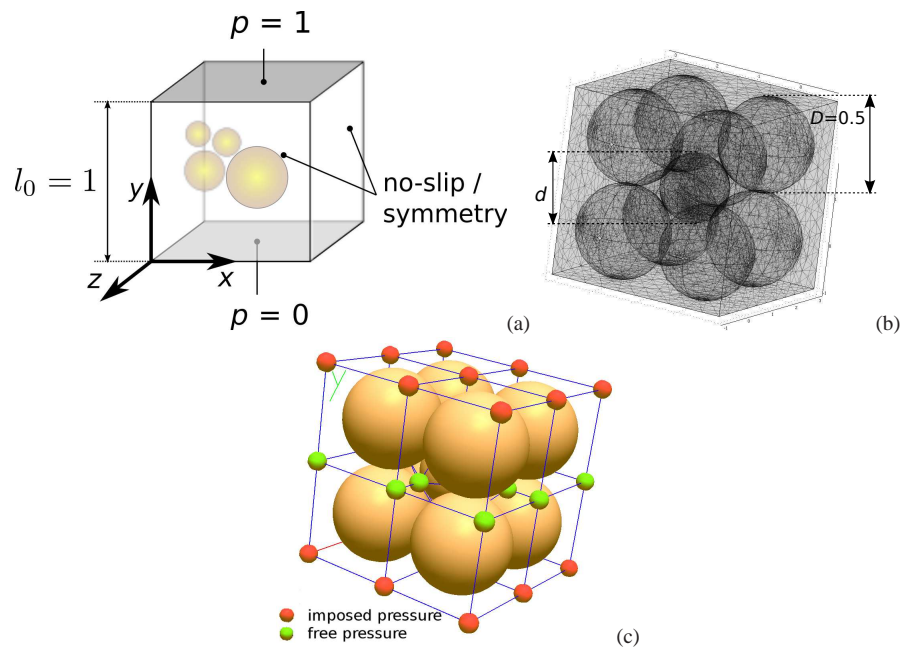


Fig. 6 Boundary conditions of flow simulations (a), FEM mesh (b) and FV mesh (c) of a 9-spheres packing. The FV packings are plotted with Voronoi graph, where pressure values are defined at each point.

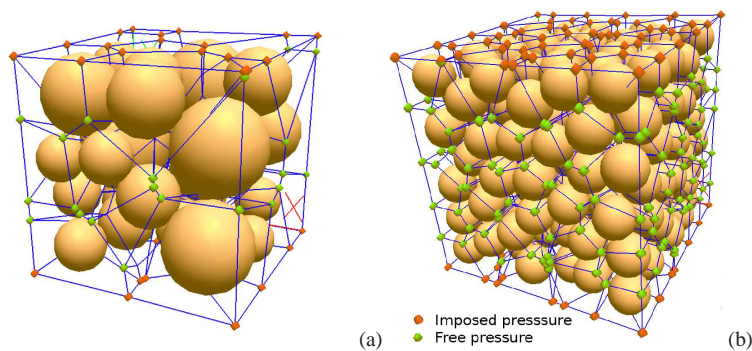


Fig. 7 Packings of 25 and 200 spheres with corresponding Voronoi graph.

Table 1 gives a comparison of problems sizes in terms of degrees of freedom (DOF) of the pressure field, and CPU times for solving. The data in this table is only an indication of how much is gained from the pore-scale formulation of Stokes flow: impacts of coarsening the FEM mesh, or benefits of other algorithms in the FV model (e.g. conjugated gradient) have not been investigated yet.

Table 1 Compared DOF's and CPU time. (a) includes only solving Stokes flow, excludes preprocessing (e.g. mesh generation) and postprocessing (forces on spheres) done via a graphical user interface; (b) includes packing triangulation, solving, and computation forces on particles; (c) out-of-memory: no result.

Nb. of spheres	FEM dof's	FV dof's	FEM (s)	time ^(a) (s)	FV (s)	time ^(b) (s)
9	1.7e5	45	300		0.00022	
200	1.2e6	1093	5400		0.0046	
2e3	(c)	11.6e3	(c)		0.091	
2e4	(c)	11.3e4	(c)		2.21	

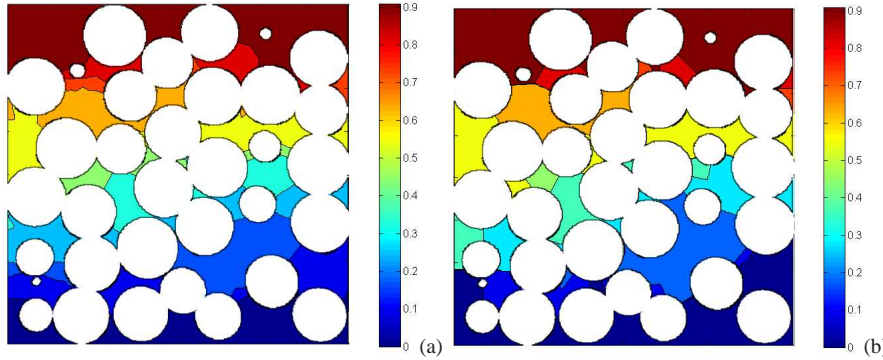


Fig. 8 Isovalues of pressure in the 200 spheres packing on the plane $x = 0.5l_0$, obtained with FEM (a) and FV (b).

3.2 Pressure Field

The pressure fields from FEM and FV are compared on figure 8. Local conductances are defined as in eqs. (8-9). The isovalues in the FV result are, by model definition (element-wise constant pressure), coincident with facets. Thus, the curvature of some isolines, as observed in FEM results, cannot be reproduced. The curvature of the isolines in the FEM solution is, however, usually very small so that most of them are reasonably approximated by straight lines. Furthermore, most isolines are found near the necks of the flow paths, thus justifying a posteriori the approximation of element-wise constant pressure used in the FV scheme. Overall, the two fields compare well. The deviation from the horizontal isolines that would be obtained in an homogeneous continuum with same boundary conditions is relatively well reproduced by the FV model.

3.3 Fluxes

Two fluxes can actually be obtained from simulations: influx Q_i , and outflux Q_o at the respective boundaries (in the FV model, they are computed by summing the q_{ij} of eq. 8 for elements where pressure is imposed). It was found that the difference between Q_i and Q_o is always negligible (less than $10^{-6} \times |Q_i|$). This is consistent with the incompressibility assumption and indicates a good convergence of the numerical solvers, be it in FEM (direct sparse solver Pardiso) or FV (Gauss Siedel method). In the following, we define $Q = Q_i$. Fluxes are expressed in the form of normalized permeability defined as $K = \mu Q h_0 / (\Delta P S^2)$,

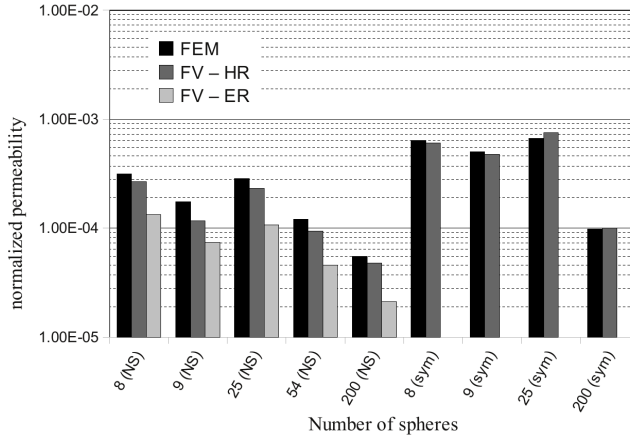


Fig. 9 Predicted permeability in FEM and FV versus size of packing, for no-slip (NS) and symmetric (sym) boundary conditions. The FV results include conductances defined using the hydraulic radius (HR - eq. 9) and effective radius (ER - eq. 10).

with $S = l_0^2$ the packing's cross-sectional area. Note that the introduction of permeability is only for the convenience of results representation, and is not implying anything with respect to the *representative volume element* (REV) concept. The topic of this paper is the comparison of small-scale modelings of fluxes and forces for some spheres packings: derivation of higher-scale properties of an equivalent continuum is beside the scope of the present investigation.

Permeabilities obtained with FEM and FV for the different packings are compared on fig. 9. Both no-slip and symmetry conditions are considered for lateral boundaries. Comparison between the definitions of conductivity using the "hydraulic" radius (HR) of eq. 9 and Bryant's "effective" radius (ER) of eq. 10 are provided. This later comparison only covers no-slip conditions, as the definition of effective radii in the symmetry case was ambiguous.

Symmetric boundary conditions give an average ratio of 1.01 between K_{HR} and K_{FEM} , with a maximum deviation of +13% for the 25-sphere packing. With no-slip conditions, the ratio are 0.78 for K_{HR}/K_{FEM} (max. deviation -40%) and 0.39 for K_{ER}/K_{FEM} (max. deviation -63%); K_{HR} is giving the best estimate of K_{FEM} in all cases. The fact that the FEM results are better reproduced for symmetric conditions suggests that the fluxes along planes are underestimated. We consider, however, that the predictions of fluxes from hydraulic radius can be considered satisfactory overall.

The evolution of permeability in 9-spheres packings as a function of size d of the inner sphere's size (fig. 6) is plotted on fig. 10. The evolution of K with d/D is correctly reflected in HR-based results. Again, FV results match FEM better for symmetric boundaries. ER-based simulations are underestimating the fluxes by an average factor $K_{ER}/K_{FEM} = 0.43$.

It can be concluded that the initial value $\alpha = 1/2$ of the conductance factor entering eq. 8 tends to underestimate fluxes in average. Although systematic comparisons could enable a better calibration of α , deviation from the FEM results is an inherent defect due to the approximations of the pore-scale description adopted here. Considering the small number of samples we tested, α has not been further adjusted to closely match FEM results.

To investigate further the differences found between K_{HR} and K_{ER} , the values of R^h and R^{eff} obtained for all facets of the 200 spheres packing triangulation have been plotted (fig 11). Clearly, the two values are strongly correlated, with the exception of very few points

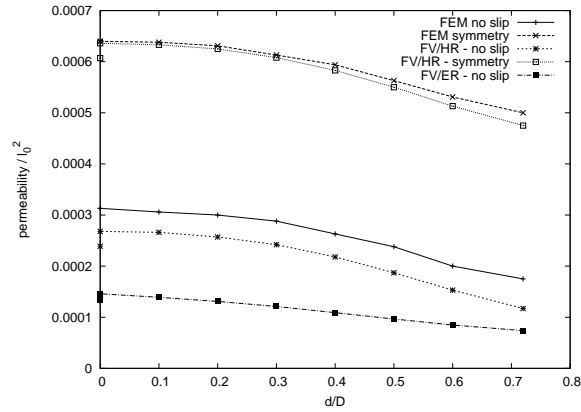


Fig. 10 Permeability of 9 spheres packing versus size of the the central particle.

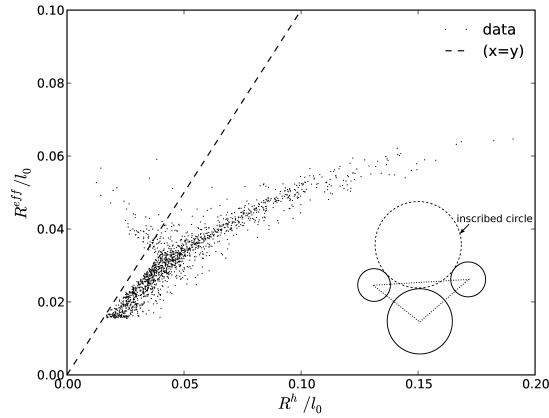


Fig. 11 Effective radius versus hydraulic radius for all facets in the 200 grains packing (a), with example of a facet giving $R_{ij}^{eff} > R_{ij}^h$.

that will be commented below, but they deviate from the $x = y$ line. The average value of R^h and R^{eff} is 1.5. Considering this distribution, it is obvious that the differences found between K_{HR} and K_{ER} are reflecting the fact that $R^h > R^{eff}$ in average at the local scale.

A small number of points fall out the well correlated cloud, for which $R^{eff} > R^h$. A close inspection of the outliers revealed that these correspond to corner cases similar to the one represented on fig. 11, where a flat triangle results in the inscribed circle overlapping outside its original facet. In such a situation, a flatter triangle will result in a smaller hydraulic radius (smaller ϕ_{ij}), but a higher effective radius. The inscribed circle will eventually overlap other inscribed circles or spheres of the packing, thus loosing physical consistency: it was not clear to us how such special cases should be handled. The number of affected facets is, however, small and do not significantly affect the results. These results lead us to conclude that the hydraulic radius is overall a more robust parameter than the effective radius.

Table 2 Normalized forces in 9 spheres packings ($d/D = 0.72$). All forces are divided by $S \cdot \Delta P$, so that the sum of all forces should be exactly 1.

	FEM	FV
<i>Forces on one big sphere (y-component)</i>		
viscous force	1.51×10^{-2}	1.06×10^{-2}
pressure force	9.09×10^{-2}	9.64×10^{-2}
total	1.06×10^{-1}	1.07×10^{-1}
<i>Forces on the small sphere (y-component)</i>		
viscous force	9.38×10^{-3}	5.83×10^{-3}
pressure force	5.17×10^{-2}	5.72×10^{-2}
total	6.04×10^{-2}	6.30×10^{-2}
<i>Forces on boundary $x=0$</i>		
viscous force (y-component)	2.27×10^{-2}	2.03×10^{-2}
pressure force (x-component)	4.98×10^{-1}	5.00×10^{-1}
<i>Total force on the solid phase</i>		
y-component	$1 - 5.56 \times 10^{-4}$	$1 + 1.18 \times 10^{-4}$

3.4 Forces

Forces on particles and boundaries, as defined in section 2.3, have been obtained for all packings using the FV scheme. In all cases, the sum of pressure and viscous forces on spheres and boundaries is, as expected, close to $\Delta P \times S$ ($\pm 10^{-5}\%$), where S is the packing's cross-sectional area. Comparison for the 8-spheres packing is trivial: $F_i = S \times \Delta P / 8$ on each sphere for both FEM and FV, modulo numerical errors. A detailed comparison is presented here only for the 9-spheres packing, for which contour integral of fluid stress in the FEM models (the FEM results in table 2 have been collected).

Table 2 gives the total fluid forces per element of the solid phase, and details the viscous and pressure contributions. The viscous force on lateral boundaries, total force on big spheres, and total force on the center sphere, are all approximated with an error smaller than 10%. Surprisingly, the prediction is less good for individual viscous and pressure contributions than for the total force. The viscous part is overestimated, while the pressure effect is underestimated. The two errors compensation results in a smaller error on the total force.

The evolution of force terms and error for the center sphere is given on fig. 12. This result shows an increasing error with decreasing d/D . For $d/D > 0.1$, the FV scheme underestimates the force on the center sphere by a factor 2. This suggest a limitation of the current formulation in the limit of (1) high contrasts in particles size, and/or (2) small particles "floating" in the voids between big ones. Here again, more investigations are needed in order to determine what situation exactly is generating this deviation from the FEM solution. As long as $d/D > 0.2$, though the predicted force is very well predicted, with error less than 10%. It is observed that similar forces are obtained with hydraulic radius (HR) and effective radius (ER).

4 Conclusion

The pore-space of a dense spheres packing can be efficiently represented by means of a regular Delaunay triangulation. In this way, the total number of DOFs and CPU time required for calculating flow and forces acting on the particles are reduced drastically with respect to small scale Stokes flow FEM calculations.

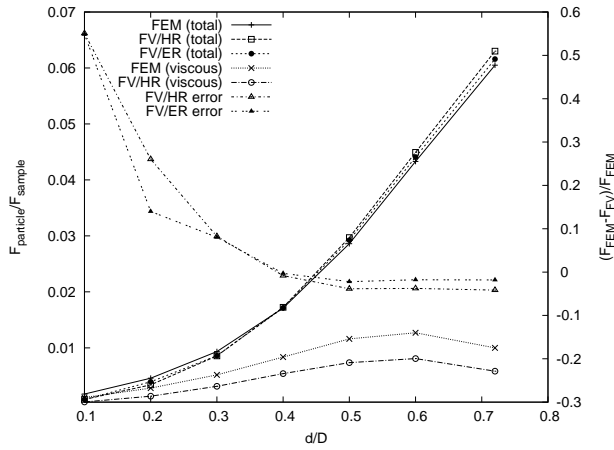


Fig. 12 Total force and viscous force applied on a particle of size d , placed in the center of a cubic packing of 8 particles of size D , in FEM simulations, FV simulations based on hydraulic radius (HR), and FV simulations based on effective radius (ER).

Expressions of local conductivities and forces induced on the particles have been derived. Bounding planes are straightforwardly taken into account in the method, and their effect in terms of permeability and viscous forces is reflected in the model for both no-slip and symmetry conditions. The method could be extended to account for non non-spherical particle shapes, as approximated by the intersection of a finite number spheres of various diameter.

The definition of local conductivity of pore throats is based on a definition of the local *hydraulic radius* R^h , as in the Kozeny-Carman (KC) derivation of permeability in porous material. The difference with KC-like derivations lies in the fact that connectivity and tortuosity of the network do not have to be included in the derivation, since they arise directly from the tetrahedral domain decomposition. The definition of the hydraulic radius R^h is simple and involves almost only real and 3D vectors multiplications for the definition of surfaces and volumes, which favors numerical performance.

Taking the FEM results as reference, the permeabilities obtained with the pore-scale modeling are in most cases within the range of $\pm 20\%$, usually below the reference value. Considering only symmetric boundary conditions, the permeabilities are better predicted (in the range $\pm 10\%$), which indicates that fluxes along planar no-slip boundaries are underestimated. We consider that such estimates are acceptable overall, keeping in mind that permeability prediction is of secondary importance, in comparison with forces, for the hydromechanical couplings.

The effective radius proposed by Bryant et al. (1993) for mono-sized spheres also gives acceptable predictions of permeabilities for polydispersed sphere packings, but it is computationally more expensive and underestimates fluid fluxes more than the hydraulic radius proposed in this investigation. It is important to note that the pore network model of Bryant et al. includes a reduction of L_{ij} , accounting for overlapping cylindrical throats. This correction has not been implemented because it needs relatively complex computations of cylinders intersections. By maximizing micro-gradients, this correction could have at least partly balanced the underestimation of permeabilities in our results. Hence, our findings cannot be considered in disagreement with Bryant et al. model in itself. They only indicate that the

effective radius should not be used in connection with the regular Delaunay partitioning we are developing.

The pressure field compares well with the FEM results. In all cases, the sum of forces applied on the solid phase in a unit cube under unit gradient is close to one, showing the correct implementation and validity of the model at the mesoscale. Forces applied by the fluid on individual particles, and viscous forces on no-slip boundaries, are found to be correct, with errors typically less than 10%: the error, though, grows larger when the size ratio d/D of the particles is less than 0.2.

This modeling of fluid forces gives a sound basis for fluid-particles systems. Current works focus on the fully coupled problems in deformable packings with deformation-induced pore pressure, and on the optimization of the flow computation in this context.

Acknowledgements This work and PhD grant of E. Catalano is supported by Grenoble Institute of Technology through BQR-2008 program. A. Cortis' work was supported, in part, by the U.S. Department of Energy under Contract N0. DE-AC02-05CH11231.

References

- T. Abichou, C. H. Benson, and T. B. Edil. Network model for hydraulic conductivity of sand-bentonite mixtures. *Can. Geotech. J.*, 41(4):698–712, 2004.
- F. Aurenhammer. Voronoi diagrams - a survey of a fundamental geometric data structure. *ACM Comput. Surv.*, 23(3):345–405, 1991.
- K. Bagi. Analysis of microstructural strain tensors for granular assemblies. *Int. J. of Solids and Structures*, 43(10):3166–3184, 2006.
- S. Bakke and P. Øren. 3-d pore-scale modelling of sandstones and flow simulations in the pore networks. *SPE Journal*, 2(2):136–149, 1997.
- J.-D. Boissonnat, O. Devillers, S. Pion, M. Teillaud, and M. Yvinec. Triangulations in CGAL. *Computational Geometry: Theory and Applications*, 22:5–19, 2002.
- R. R. O. Bonilla. *Numerical simulation of undrained granular media*. PhD thesis, University of Waterloo, 2004.
- S. Bryant and M. Blunt. Prediction of relative permeability in simple porous media. *Phys. Rev. A*, 46(4):2004–2011, 1992.
- S. Bryant and A. Johnson. Wetting phase connectivity and irreducible saturation in simple granular media. *J. of Colloid and Interface Science*, 263(2):572–579, 2003.
- S. Bryant, P. King, and D. Mellor. Network model evaluation of permeability and spatial correlation in a real random sphere packing. *Transp. Porous Med.*, 11(1):53–70, 1993.
- F. Calvetti, G. Combe, and J. Lanier. Experimental micromechanical analysis of a 2d granular material: relation between structure evolution and loading path. *Mech. Cohes.-Fric. Mater.*, 2(2):121–163, 1997.
- B. Chareyre, L. Briançon, and P. Villard. Theoretical versus experimental modelling of the anchorage capacity of geotextiles in trenches. *Geosynthetics International*, 9(2):97–123, 2002.
- P. Cundall and O. Strack. A discrete numerical model for granular assemblies. *Geotechnique*, (29):47–65, 1979.
- H. Edelsbrunner and N. R. Shah. Incremental topological flipping works for regular triangulations. *Algorithmica*, 15(6):223–241, 1996.

- R. Glowinski, T. W. Pan, T. I. Hesla, D. D. Joseph, and J. Periaux. A fictitious domain approach to the direct numerical simulation of incompressible viscous flow past moving rigid bodies. *J. of Computational Phys.*, 169(2):363–426, 2001.
- M. Hakuno. Simulation of the dynamic liquefaction of sand. In *Earthq. geotechnical engineering*, pages 857–862. Balkema, 1995.
- M. Hilpert, R. Glantz, and C. T. Miller. Calibration of a pore-network model by a pore-morphological analysis. *Transp. Porous Med.*, (51):267–285, 2003.
- J.-F. Jerier, B. Hathong, V. Richefeu, B. Chareyre, D. Imbault, F.-V. Donze, and P. Doremus. Study of cold powder compaction by using the discrete element method. *Powder Tech.*, In Press, 2010. doi: DOI:10.1016/j.powtec.2010.08.056.
- K. D. Kafui, C. Thornton, and M. J. Adams. Discrete particle-continuum fluid modeling of gas-solid fluidized beds. *Chem. Eng. Sci.*, 57(13):2395–2410, july 2002.
- T. Kawaguchi, T. Tanaka, and Y. Tsuji. Numerical simulation of two-dimensional fluidised beds using the discrete element method (comparison between two- and three-dimensional models). *Powder Tech.*, 96:129–138, 1998.
- Y. Liu and J. Snoeyink. A comparison of five implementations of 3d delaunay tessellation. In J. Pach, J. E. Goodman, and E. Welzl, editors, *Combinatorial and Computational Geometry*, pages 439–458. MSRI Publications, 2005.
- V. A. Luchnikov, N. N. Medvedev, L. Oger, and J.-P. Troadec. Voronoi-delaunay analysis of voids in systems of nonspherical particles. *Phys. Rev. E*, 59(6):7205–7212, Jun 1999.
- S. McNamara, E. G. Flekkøy, and K. J. Måløy. Grains and gas flow: Molecular dynamics with hydrodynamic interactions. *Phys. Rev. E*, 61(4):4054–4059, Apr 2000.
- N. Mortensen, F. Okkels, and H. Bruus. *Phys. Rev. E*, 71(5):057301, 2005.
- H. Nakasa, T. Takeda, and M. Oda. A simulation study on liquefaction using dem. In *Earthquake geotechnical engineering*, pages 637–642. Balkema, 1999.
- M. J. Niebling, E. G. Flekkøy, K. J. Måløy, and R. Toussaint. Sedimentation instabilities: Impact of the fluid compressibility and viscosity. *Phys. Rev. E*, 82(5):051302, Nov 2010.
- A. V. Oostroom and J. Strackee. The solid angle of a plane triangle. *IEEE Trans. on Biomedical Eng.*, BME-30(2):125–126, 1983.
- P. Øren, S. Bakke, and O. Arntzen. Extending predictive capabilities to network models. *SPE Journal*, 3(4):324–336, 1998.
- T. Patzek and T. Silin. Shape factor and hydraulic conductance in noncircular capillaries: I. one-phase creeping flow. *J. of Colloid and Interface Science*, 236(2):295–304, 2001.
- M. Piri and M. J. Blunt. Three-dimensional mixed-wet random pore-scale network modeling of two- and three-phase flow in porous media. i. model description. *Phys. Rev. E*, 71(2): 026301, Feb 2005.
- E. Sanchez-Palencia and A. Zaoui, editors. *Homogenization Techniques for Composite Media*, volume 272 of *Lecture Notes in Physics*, Berlin Springer Verlag, 1987.
- L. Scholtes, P.Y. Hicher, F. Nicot, B. Chareyre, and F. Darve. On the capillary stress tensor in wet granular materials. *Int. J. Numer. Anal. Meth. Geomech.*, 33(10):1289–1313, 2009.
- V. Smilauer, E. Catalano, B. Chareyre, S. Dorofeenko, J. Duriez, A. Gladky, J. Kozicki, C. Modenese, L. Scholtes, L. Sibille, J. Stransky, and K. Thoeni. Yade Reference Documentation. In V. Smilauer, editor, *Yade Documentation*. 2010. <http://yade-dem.org/doc/>.
- K. E. Thompson and H. S. Fogler. Modeling flow in disordered packed beds from pore-scale fluid mechanics. *AIChE Journal*, 43(6):1547–5905, 1997.
- S. Whitaker. *The method of volume averaging*. Kluwer Netherlands, 1999.
- M. Zeghal and U. E. Shamy. A continuum-discrete hydromechanical analysis of granular deposit liquefaction. *Int. J. Numer. Anal. Meth. Geomech.*, 28(14):1361–1383, 2004.